
Image-based Treatment Effect Heterogeneity

Connor T. Jerzak

Institute for Analytical Sociology
Linköping University
Email: connor.jerzak@liu.se
Website: ConnorJerzak.com

Fredrik Johansson

Data Science and AI Division
Chalmers University of Technology
Email: fredrik.johansson@chalmers.se
Website: fredjo.com

Adel Daoud

Institute for Analytical Sociology
Linköping University
Email: adel.daoud@liu.se
Website: AdelDaoud.se
AI and Global Development Lab: global-lab.ai

Abstract

Randomized controlled trials (RCTs) are considered the gold standard for estimating the effects of interventions. Recent work has studied effect heterogeneity in RCTs by conditioning estimates on tabular variables such as age and ethnicity. However, such variables are often only observed near the time of the experiment and may fail to capture historical or geographical reasons for effect variation. When experiment units are associated with a particular location, satellite imagery can provide such historical and geographical information, yet there is no method which incorporates it for describing effect heterogeneity. In this paper, we develop such a method which estimates, using a deep probabilistic modeling framework, the clusters of images having the same distribution over treatment effects. We compare the proposed methods against alternatives in simulation and in an application to estimating the effects of an anti-poverty intervention in Uganda. A causal regularization penalty is introduced to ensure reliability of the cluster model in recovering Average Treatment Effects (ATEs). Finally, we discuss feasibility, limitations, and the applicability of these methods to other domains, such as medicine and climate science, where image information is prevalent. We make code for all modeling strategies publicly available in an open-source software package.

1 Introduction

Field experiments in the social and health sciences help us understand the effects of interventions in the natural habitat where people live (Banerjee et al., 2011). Their primary goal is often to identify the average effect (ATE) of a treatment T_i on an outcome Y_i over units i in a population. By collecting tabular characteristics, \mathbf{X}_i , such as age, sex, and income, researchers may estimate Conditional Average Treatment Effects (CATEs) to analyze effects by sub-populations (Künzel et al., 2019; Balgi et al., 2022), and thereby, to optimize treatments for each group. But, the features in \mathbf{X}_i are often measured only at baseline, just before the experiment is initiated. Thus, \mathbf{X}_i tend to miss critical historical and geographical characteristics for treatment optimization (Kino et al., 2021).

When units i are associated with a particular location, satellite images, \mathbf{M}_i , can provide missing historical and geographical context (Burke et al., 2021; Daoud et al., 2021). In contrast to covariates measured during experiments, satellite imagery is routinely collected passively from space. These data have been collected for parts of the world since the CORONA intelligence satellites of the 1950s

and for the entire world since the start of the Landsat mission in 1970s. The Landsat data are publicly available, with revisiting time of ~ 16 days. By combining satellite imagery with experimental data, researchers can investigate not only the historical and geographical roots of effect variation, but they can also analyze how an intervention might impact places outside the scope of the original study. Such analysis are made possible as imagery can be obtained not only for the experimental setting but also places not originally in the experiment and where no background covariates were measured. This possibility would potentially increase the applicability of casual transportability to a considerable degree (Pearl and Bareinboim, 2022). Nonetheless, despite the potential offered by images for causal inference (Castro et al., 2020; Chalupka et al., 2016b,a, 2015; Schölkopf et al., 2021; Yi et al., 2020; Ding et al., 2021; Paciorek, 2010; Kaddour et al., 2021b; Louizos et al., 2017; Pawlowski et al., 2020; Lopez-Paz et al., 2017), it remains unclear how researchers should use these \mathbf{M}_i for CATE analysis. The two main interrelated challenges are that \mathbf{M}_i is high-dimensional and often not annotated: thus, a CATE analysis based on \mathbf{M}_i could have poor interpretability.

In this article, we develop models which identify treatment effect heterogeneity in data from randomized controlled trials (RCTs) by analyzing satellite imagery collected independently of the experiments. The probabilistic models we develop employ Bayesian convolutional neural network arms (CNNs) and categorical gates that allow us to directly model mixtures of image clusters with similar effects. That is, our models estimate treatment effects for all units, conditional on treatment status, the images \mathbf{M}_i , and, if desired, accounting for available \mathbf{X}_i through orthogonalization. (By residualizing, our model will identify what additional CATE dynamics that stem from \mathbf{M}_i , separately from \mathbf{X}_i). The models construct clusters that categorize units based on their Image-Type CATE similarity.

In the following sections, we develop our methods, show some properties analytically, and explore others in simulated experiments. We demonstrate its usefulness by replicating the results of an RCT study in Uganda—the Youth Opportunities Program (YOP) (Blattman et al., 2014). This study, conducted in 2008, was designed to help the poor break unemployment cycles by assisting their artisans and business activity. The government solicited young adults to participate in YOP, asking them to form teams and compose a business plan. After screening these teams and their plans, the government randomly assigned a one-time grant worth about \$7,500 to each team. This amount equals approximately their joint annual income. Most of the applicants were rural farmers, which had low educational attainment (\sim eighth grade), earned less than \$1 per day, and worked less than twelve hours per week. As many RCTs like YOP, the researchers collected a set of baseline covariates, but none of them capture past historical or geographical characteristics. Our replication analysis demonstrates the benefits, and limitations, of using \mathbf{M}_i for CATE, as a complement to \mathbf{X}_i .

While our contribution focuses on the use of satellite images in global poverty research, our methods are designed such that they can be generalized to other forms of RCTs where complementary image data is available. In the last few decades, there has been a rapid increase in the availability of imaging technologies. Most notably, these technologies are readily available in medicine, epidemiology and adjacent fields, using X-ray, positron emission, MRI, and ultrasound. We hypothesize that these images are useful not only for estimating ATE (Castro et al., 2020; Lopez-Paz et al., 2017; Chalupka et al., 2016b), but also for evaluating CATE. Nonetheless, more research is required to systematically evaluate our models generalizability for these domains.

2 Background and Related Work

Conditional Average Treatment Effects with Tabular Data Let $Y_i(t)$ denote the potential outcome (Rubin, 2005) of an intervention $t \in \{0, 1\}$ for a unit of study i . For example, $Y_i(1)$ may represent the poverty level in a household i following an aid intervention, and $Y_i(0)$ the level without intervention. We may define the unit-level treatment effect as

$$\text{Individual Treatment Effect: } \tau_i = Y_i(1) - Y_i(0).$$

When τ_i is greater than 0, the unit’s outcome is greater under treatment than otherwise. Without conducting counterfactual inference (Pearl, 2009), the quantity τ_i cannot be identified, because only either of the potential outcomes $Y_i(1)$ or $Y_i(0)$ are observed: a unit can only receive a single treatment at a given time, and thus, the counterfactual remains unobserved. Assuming consistency Hernán MA (2020), the observed outcome can be written, $Y_i = Y_i(T_i) = Y_i(1)T_i + Y_i(0)(1 - T_i)$, where T_i denotes the (random) treatment status of i . The ATE captures the population effect by averaging over

all unit-level effects:

$$\text{Average Treatment Effect (ATE): } \bar{\tau} = \mathbb{E}[\tau_i] = \mathbb{E}[Y_i(1) - Y_i(0)].$$

The ATE is useful as it marginalizes over the heterogeneity present in a population to form an overall assessment of an experiment. In an RCT, due to treatment randomization, ATE can be estimated non-parametrically by the difference between treatment and control outcomes (Rubin, 2005),

$$\hat{\tau}_{\text{Non-parametric}} = n_1^{-1} \sum_{i=1}^n Y_i \cdot T_i - n_0^{-1} \sum_{i=1}^n Y_i \cdot (1 - T_i),$$

where n_t denotes the number of units in treatment group, $t \in \{0, 1\}$. Despite the importance of aggregate quantities such as the ATE, it is useful to disaggregate average effects using based on contextual information. Such a disaggregation is critical for not only scientific understanding but also for policy (e.g., personalizing treatments (Greenland et al., 2020; Balgi et al., 2022)) and industry applications (e.g., personalizing advertisement (Nabi et al., 2020)). This disaggregation can be a function of any type of general pre-treatment data variable, \mathbf{G}_i :

$$\text{Conditional Average Treatment Effect (CATE): } \tau(\mathbf{g}) = \mathbb{E}[Y_i(1) - Y_i(0) \mid \mathbf{G}_i = \mathbf{g}],$$

The literature has primarily focused on conditioning sets which contain tabular data, \mathbf{X}_i :

$$\text{Tabular Conditional Average Treatment Effect: } \tau(\mathbf{x}) = \mathbb{E}[Y_i(1) - Y_i(0) \mid \mathbf{X}_i = \mathbf{x}],$$

where $\mathbf{x} \in \mathbb{R}^D$ denotes the vector of D pre-treatment covariates (Athey and Imbens, 2016; Athey et al., 2019; Ding et al., 2016; Imai and Ratkovic, 2013; Shalit et al., 2017; Zhao et al., 2017; Luedtke and van der Laan, 2016; Nie and Wager, 2021). For example, the generalized random forest is one such recent machine-learning method (Athey et al., 2019) that has proven useful in a variety of applied settings (Shiba et al., 2021; Daoud and Johansson, 2019). These methods are tailored for annotated tabular data, but images are high-dimensional and often not annotated. These non-annotated image features consists of image bands and pixels that may jointly induce effect heterogeneity. In the remainder of this paper, we focus on improving the ability of investigators to understand treatment effect heterogeneity in the context of unstructured high-dimensional image data.

Causal Inference with Image Data While most studies estimating causal effects use tabular data, there is an increasing realization that image data provides a creative yet useful way to conduct causal inference (Castro et al., 2020; Ramachandra, 2019; Daoud and Dubhashi, 2020). To this end, there has been some methodological development, investigating how images should be integrated to identify and estimate ATEs in the observational setting (Kallus, 2020; Kaddour et al., 2021a; Pawlowski et al., 2020; Jerzak et al., 2022). Here, images are part of the adjustment set. Therefore, most methodological development has focused on how to use images to proxy confounding variables; less is known about how to use images for CATE estimation.

As discussed in §1, images may provide critical information for effect understanding. Like any tabular information in \mathbf{X}_i , images as a whole or through segments may modify effects. In the observational setting, images \mathbf{M}_i could both be part of the conditioning set and the effect modification set. In the RCT setting, \mathbf{M}_i is not a confounder (and thus, unnecessary to identify ATE), since the treatment was randomized. In both settings, one target estimand is the Image CATE,

$$\text{Image CATE: } \tau(\mathbf{m}) = \mathbb{E}[Y_i(1) - Y_i(0) \mid \mathbf{M}_i = \mathbf{m}],$$

where $\mathbf{m} \in \mathbb{R}^{W \times H \times D}$ is an image, obtained from prior to the assignment of treatment, of width W , height H , and with D data channels. These data channels often correspond to reflectance information from various bands. While Image and Tabular CATEs are both a subset of the general CATEs, there are conceptual differences. First, by their nature, images are unstructured, high dimensional objects. In RCT applications, every image will likely be unique as image effects act much as individual-level treatment effects, where summarizing the quantity of interest becomes increasingly difficult with a growing number of units. Second, as unstructured, it may be unclear how to interpret the act of conditioning on an image. We need a conceptual language and modeling strategy for understanding “closeness” between images in the space of conditional effects. The rest of our article contributes to establishing this conceptual language, focusing for the sake of clarity on the RCT setting.

3 Modeling Causal Effect Heterogeneity in Images

In experimental settings, CATEs may be estimated readily by function approximation. Perhaps the simplest approach is to fit a separate model, $\hat{Y}_t(\mathbf{m})$, to observations of the potential outcome $Y(t)$ of each intervention—a so-called *T-learner* (Künzel et al., 2019). The CATE may then be estimated as $\hat{\tau}(\mathbf{m}) = \hat{Y}_1(\mathbf{m}) - \hat{Y}_0(\mathbf{m})$. Shalit et al. (2017) found that learning a shared representation Φ used to predict both treatment outcomes improved prediction quality and dubbed this approach TARNet.

Given any model of heterogeneity $\hat{\tau}$, we can partition units by their predicted causal effect, creating a clustering of inputs *post hoc*. Let $C(\hat{\tau}(m)) \in \{1, 2, \dots, K\}$ denote a cluster labeling function determined by the output of $\hat{\tau}$, which partitions the space of effect sizes and, as a result, the space of images. C may be constructed by uniform binning of $\hat{\tau}$, quantile binning or, as in our experiments, by k -means clustering. Then, the CATE with respect to the post-hoc clustering labels is

$$\text{Prediction Cluster CATE: } \tau(c) = \mathbb{E}[Y_i(1) - Y_i(0) \mid C(\hat{\tau}(\mathbf{M}_i)) = c],$$

In our experiments, we use the post-hoc clustering of TARNet’s $\hat{\tau}(\mathbf{M}_i)$ estimates as baseline.

A drawback of the post-hoc model is that it compounds approximations to arrive at a small discrete representation of treatment effect heterogeneity. If two similar images yield very different predictions due to misestimation, they are likely to be placed in different clusters. Instead, we would prefer to cluster images smoothly in a way which best approximates treatment effect heterogeneity. Moreover, it is difficult to quantify the aggregation of uncertainty in post-hoc clustering, especially as it may be difficult to propagate gradients through both the outcome and subsequent clustering model.

3.1 Probabilistic Effect Clustering Based on Image Type

With these observations in mind, we develop a modeling strategy for summarizing treatment effect heterogeneity that is driven by image patterns which can be succinctly summarized for the purposes of interpretability. To the best of our knowledge, this is the first work to use images to summarize causal effect heterogeneity, so we will strive for simplicity in our model and application.

The primary criteria our modeling strategy needs to fulfil are: (1) *model potential outcomes and treatment effects flexibly* and (2) *identify interpretable image clusters with similar in-cluster effect sizes, and different cross-cluster effects*. Our target quantity of interest will be

$$\text{Image-Type CATE: } \tau(z) = \mathbb{E}[Y_i(1) - Y_i(0) \mid Z_i = z],$$

where $Z_i \in \{1, 2, \dots, K\}$ denotes the effect cluster of image \mathbf{M}_i , where there are K total clusters. We will search for assignments Z_i of clusters to images that best explains treatment effect variation. Perhaps the closest existing analogue to this quantity is the mixture of experts approach for CATEs in the conjoint setting using linear models with interactions (Goplerud et al., 2022).

Because the treatment effects are decomposed by image type, there are only K quantities needed to effectively summarize the heterogeneity accountable to images. Since human working memory can track between 3 to 5 distinct chunks at any single time (Cowan, 2010), this summary of the complex heterogeneity process stemming from images can in principle be represented in stakeholders’ mental processes, so long as the number of image effect types is reasonably small. This possibility is important because it may facilitate the communication and effective implementation of future treatment targeting decisions. With this substantive motivation in mind, we now discuss how we fulfil the two modeling criteria in pursuit of understanding treatment effect heterogeneity with images.

Effect Mixture Based on Image Type We satisfy the first criterion by allowing the baseline potential outcome, $Y_i(0)$, to be estimated flexibly as a function of the image. In particular, we let the mean of the baseline potential outcome, conditional on the image, be parameterized by a Bayesian convolutional neural network,

$$\mathbb{E}[Y_i(0) \mid \mathbf{M}_i = \mathbf{m}] = \{\mu_{Y_i(0)} \mid \mathbf{M}_i = \mathbf{m}\} \sim \text{Bayesian CNN}(\mathbf{m}).$$

We employ a Bayesian network, where convolutional and dense parameters are not deterministic, but instead defined according to a distribution. This will allow us to explicitly explore uncertainty in the implied Image-Type CATEs. Use of Bayesian networks (or approximations thereof, e.g., dropout) has also empirically been observed to help prevent overfitting (Gal and Ghahramani, 2016), an important

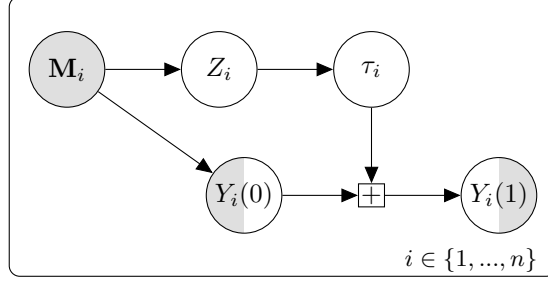


Figure 1: Stylized schematic depiction of the probabilistic treatment heterogeneity model for images. The gray circles denote observed random variables; the white circles denote latent variables; the mixed gray/white nodes denote partially observed nodes (i.e. variables which are observed for some, but not all, units). Square node denotes deterministic transformations that operate on the means for each input node (see text). Z_i denotes the image type generating a distribution over treatment effects.

property in the case of experiments implemented by governments or international organizations, where the number of experimental units may be relatively small ($\sim 10^3$).

Having flexibly defined the baseline, we turn our attention to the Image-Type CATE estimand, using two alternative models. Our first model computes image type probabilities \mathbf{P}_i using another Bayesian network. Conditional on the *image type* $Z = z$, treatment effects are drawn assumed to be Normally distributed with a unique mean $\mu_{\tau,z}$ and variance $\sigma_{\tau,z}^2$ indexed to that image type. We do not assume that there is a single treatment effect per image type, but instead that there is a specific distribution over treatment effects by image type. The cluster effect means and variances offer a complete summarization of this distribution. The assumed probabilistic generative model for image-based treatment effect heterogeneity is summarized in Figure 1 and defined in full below

$$\begin{aligned}
 & \text{Generating the Image Type} \\
 & \{\mathbf{P}_i \mid \mathbf{M}_i = \mathbf{m}\} \sim \text{Bayesian CNN}(\mathbf{m}) \\
 & \{Z_i \mid \mathbf{P}_i = \mathbf{p}\} \sim \text{Categorical}(\mathbf{p}) \\
 & \downarrow \\
 & \text{Generating the Treatment Effect Distributions} \\
 & \text{Image-Type Effect Cluster Model (§3.1): } \{\tau_i \mid Z_i = z\} \sim \mathcal{N}(\mu_{\tau,z}, \sigma_{\tau,z}^2) \\
 & \text{Image-Type Differential Effect Model (§3.1): } \{\tau_i \mid \mathbf{M}_i = \mathbf{m}, Z_i = z\} \sim \text{Bayesian CNN}(z)(\mathbf{m}) \\
 & \downarrow \\
 & \begin{array}{ll}
 \text{Generating the Baseline Outcome, } Y_i(0) & \text{Generating the Outcome under Treatment, } Y_i(1) \\
 \{\mu_{Y_i(0)} \mid \mathbf{M}_i = \mathbf{m}\} \sim \text{Bayesian CNN}(\mathbf{m}) & \rightarrow \{Y_i(1) \mid \mu_{Y_i(0)}, \tau_i, \sigma_{1,z}^2\} \sim \mathcal{N}(\mu_{Y_i(0)} + \tau_i, \sigma_{1,z}^2) \\
 \{Y_i(0) \mid \mu_{Y_i(0)}, \sigma_{0,z}^2\} \sim \mathcal{N}(\mu_{Y_i(0)}, \sigma_{0,z}^2) &
 \end{array}
 \end{aligned}$$

In this approach, the treatment effects decomposed by treatment type are variational parameters. By the structure of the model outlined in Figure 1, we have conditional mean and variance (see A.1.1),

$$\tau(z) = \mathbb{E}[Y_i(1) - Y_i(0) \mid Z_i = z] = \mu_{\tau,z}, \quad \text{Var}(Y_i(1) - Y_i(0) \mid Z_i = z) = \sigma_{0,z}^2 + \sigma_{1,z}^2 + \sigma_{\tau,z}^2.$$

Besides the enhanced interpretability from summarizing image-derived effect heterogeneity in K discrete clusters, there are other advantages to our modeling strategy. First, as it is probabilistic, we can explore uncertainty not only in the treatment effects by also in the cluster assignment probabilities. Second, the image type decomposition also may facilitate scientific inquiry: the image type serve as natural generalization of the image, facilitating theorizing about the causal mechanisms at play. Third, we can readily compute the gradients of the cluster probabilities with respect to the image in order to identify *how* the image affects the typology (see §3.3).

Using the model outlined in Figure 1, we seek to learn the joint distribution of the model parameters Θ and the image clustering, \mathbf{Z} , given the observed dataset, $\mathbf{D} = \{Y_i(T_i), \mathbf{M}_i, T_i\}_{i=1}^n$:

$$\text{Target Posterior: } p(\mathbf{Z}, \Theta \mid \mathbf{D}), \quad (1)$$

where $\mathbf{Z} = \{Z_i\}_{i=1}^n$. For additional details of how we model the uncertainties, see A.1. To estimate the posterior in (1), we maximize the Evidence Lower Bound (ELBO) (Ranganath et al., 2014),

$$\begin{aligned} \underset{q(\mathbf{Z}, \boldsymbol{\Theta} | \mathbf{M}, \mathbf{T})}{\text{maximize}} \quad & \mathbb{E}_{q(\mathbf{Z}, \boldsymbol{\Theta} | \mathbf{M}, \mathbf{T})} [\log (p(\mathbf{Y}(\mathbf{T}) | \mathbf{Z}, \boldsymbol{\Theta}, \mathbf{M}, \mathbf{T}))] \\ & - D_{\text{KL}} (q(\mathbf{Z}, \boldsymbol{\Theta} | \mathbf{M}, \mathbf{T}) || p(\mathbf{Z}, \boldsymbol{\Theta} | \mathbf{M}, \mathbf{T})). \end{aligned}$$

We solve the problem approximately using stochastic gradient descent with gradients passing through discrete sampling nodes using re-parameterization techniques (Parmas and Sugiyama, 2021). An additional benefit of the approach proposed here, as opposed to post-hoc clustering, is that uncertainty of the variational clustering model can be quantified using M -estimation theory (Westling and McCormick, 2019). Also, choice of priors affects finite sample performance, so when possible, we specify priors using empirically observable marginal information (e.g., the prior mean for the cluster effects is set to $\hat{\tau}_{\text{Non-parametric}}$).

Differential Effects Based on Image Type The first effect mixture model we introduced could be useful to investigators because conditional effects can be succinctly summarized, but in some circumstances, investigators may seek a more flexible modeling strategy for $Y_i(1)$. In that case, the distribution of treatment effects given the image type z is parameterized by a Bayesian CNN arm indexed to z :

$$\{\tau_i | \mathbf{M}_i = \mathbf{m}, Z_i = z\} \sim \text{Bayesian CNN}(z)(\mathbf{m})$$

In essence, the image type acts as a stochastic gate which determines which image patterns will be used in predicting the treatment effect.

3.2 Encouraging Unbiased ATE Estimates via Causal Regularization

The modeling process just described involves selecting several parameters, such as the number of clusters and even the kind of images used. Given the numerous possibilities involved, we propose the addition of a causal regularization term to encourage all models to be equivalent in their implied marginal effect (for discussion of causal regularization in a different context, see (Oberst et al., 2021)). That is, by the Law of Total Expectation, the ATE $\bar{\tau}$ satisfies

$$\bar{\tau} = \mathbb{E}[Y_i(1) - Y_i(0)] = \sum_{z=1}^K \mathbb{E}[Y_i(1) - Y_i(0) | Z_i = z] \Pr(Z_i = z) = \sum_{z=1}^K \tau(z) \Pr(Z_i = z),$$

a fact which gives rise to a natural estimator using the sample analogues of the theoretical quantities: $\hat{\tau}_{\text{Model}} = \sum_{z=1}^K \hat{\tau}(z) \hat{\Pr}(Z_i = z)$, where the $\hat{\tau}(z)$'s are taken from the mixture components and the $\hat{\Pr}(Z_i = z)$ term is estimated from the marginal cluster probabilities.

However, as noted, the ATE can also be estimated using the non-parametric difference-in-means estimator described in §2, with estimation being, under minimal assumptions, consistent (Imbens and Rubin, 2015). Thus, if the proposed heterogeneity model is consistent as well,

$$\{\hat{\tau}_{\text{Model}} \xrightarrow{n \rightarrow \infty} \bar{\tau}\}, \{\hat{\tau}_{\text{Non-parametric}} \xrightarrow{n \rightarrow \infty} \bar{\tau}\} \Rightarrow (\hat{\tau}_{\text{Model}} - \hat{\tau}_{\text{Non-parametric}})^2 \xrightarrow{n \rightarrow \infty} 0 \quad (2)$$

If the implied ATE from the model diverges too far from the non-parameteric estimator, the credibility of the proposed model would be thereby reduced. Under additional modeling assumptions, we can in fact re-parameterize the parametric model exactly so that $\hat{\tau}_{\text{Model}} = \hat{\tau}_{\text{Non-parametric}}$ exactly (see A.2). However, the exact re-parameterization forcing $\hat{\tau}_{\text{Model}} = \hat{\tau}_{\text{Non-parametric}}$ involves similar problems as found in the compositional statistics literature (e.g., ordering of clusters can affect the results (Greenacre, 2021)), we instead incorporate a soft penalty that is invariant to the ordering of clusters:

$$\text{Model ATE Equivalence Regularization Term: } \lambda \left(\sum_{z=1}^K \hat{\tau}(z) \hat{\Pr}(Z_i = z) - \hat{\tau}_{\text{Non-parametric}} \right)^2$$

We add this to the variational objective to encourage marginal effects to be equivalent regardless of the parameterization of the model, using a non-parametric estimator for the ATE as a baseline.

3.3 Determination of Sensitivity Regions

One benefit of the proposed probabilistic image-type heterogeneity decomposition is that we can examine the model in order to assess how image information translates into the predicted effect cluster. In particular, we take the derivative of the cluster probabilities with respect to pixels (i, w, h) :

$$s_{iwh} = \sum_{d=1}^D \sum_{z=1}^K \left| \frac{\partial \widehat{\Pr}(Z_i = z \mid \mathbf{M}_i = \mathbf{m})}{\partial m_{whd}} \right|$$

Large values of s_{iwh} reveal locations in the image that, if changed, would lead to the large changes in the cluster probabilities; s_{iwh} can thus provide a basis for understanding how image information translates into the effect typology. This sensitivity information is difficult to compute for post-hoc clustering methods, as the clustering of the $\hat{\tau}_i$'s needs to solve a second optimization problem (as in k -means) through which gradients w.r.t. the initial outcome model(s) may not be efficiently traced.

3.4 Policy Action Using the Image-based Heterogeneity Model

A major motivation for considering image-based CATEs is that we can readily generate predictive distributions over treatment effects for contexts outside the experimental setting and where no tabular covariates were measured by researchers. In this context, for a new out of sample point, $i \in \mathcal{I}(\text{Out})$, we form a predictive distribution over image treatment effects using

$$p(\tau_i \mid \mathbf{M}_i, \mathbf{D}) = \sum_{z=1}^K \int p(\tau_i \mid Z_i = z; \boldsymbol{\Theta} = \boldsymbol{\theta}) \cdot p(Z_i = z \mid \mathbf{M}_i; \boldsymbol{\Theta} = \boldsymbol{\theta}) \cdot p(\boldsymbol{\Theta} = \boldsymbol{\theta} \mid \mathbf{D}) d\boldsymbol{\theta}$$

We can use the predictive distribution over treatment effects to improve treatment targeting for out-of-sample individuals. With a fixed treatment budget of size n_1^O for the new dataset of size $n^O = |\mathcal{I}(\text{Out})|$, this policy can be written as $\Pi(\{\mathbf{M}_i\}_{\mathcal{I}(\text{Out})}) \rightarrow \{0, 1\}^{n^O}$. There are many approaches to this out-of-sample treatment targeting and we refer readers to that literature (Hitsch and Misra, 2018).

3.5 Distinguishing Image from Tabular Conditional Effects

In some contexts, like when tabular covariates are not measured or when we seek to generate predictions for contexts without tabular covariates, it may be particularly useful to perform image-type effect clustering directly using the images. However, when other tabular covariates are measured for the sample and only that sample is of interest, researchers may seek to understand the heterogeneity stemming from image information that is not redundant vis-à-vis tabular covariates.

For example, race is correlated with the image information of neighborhoods in the United States, where minorities are concentrated in dense urban centers with little green space while more affluent non-minorities tend to live in green-space rich areas outside cities (Cucca, 2020). We might naturally ask about the remaining heterogeneity after accounting for the heterogeneity due to key tabular variables such as race. We therefore can perform the image clustering on the orthogonalized outcomes:

$$Y_i(t)^\perp = Y_i(t) - \widehat{\mathbb{E}}[Y_i(t) \mid \mathbf{X}_i].$$

The resulting clusters, estimated using the modeling strategies in §3.1, then can be interpreted as image effect clusters after accounting for the heterogeneity present in the measured tabular data.

4 Treatment Effect Cluster Recovery in Simulation

We now explore dynamics of the proposed methods via simulation, where true effects are known.

Design We generate image-based treatment effect heterogeneity using,

$$H_i = \text{GN}(\max(f_l(\mathbf{M}_i))), \quad H_i^+ = \underbrace{|\min\{H_i\}_{i=1}^n|}_{\text{Ensures } \tau_i > 0} + \underbrace{\text{sign}(H_i) \cdot |H_i|^{1/\gamma}}_{\text{Generates bimodality as } \gamma \rightarrow \infty} \quad (3)$$

where $f_l(\cdot)$ denotes the application of a $l \times l$ filter to the image, $\max(\cdot)$ denotes the global maximum operation across the image, and $\text{GN}(\cdot)$ denotes a global normalization function scaling

the H_i values to have mean 0 and variance 1 across the image pool. The specific transformation generating H_i^+ is selected (1) to ensure all the treatment effects are in the same direction (i.e. all positive) and (2) to generate heterogeneity in the effect distribution, with greater bimodality in the treatment response as $\gamma \rightarrow \infty$. We let $\gamma = 2$. We define the treatment and outcome:

$$T_i \sim \text{Binomial}(0.5), \quad Y_i = T_i H_i^+ + \epsilon_i,$$

with $\epsilon_i \sim \mathcal{N}(0, \nu \cdot \text{Var}(H_i^+))$. The value of ν controls the extent to which the image is predictive of the outcomes, where smaller values indicate stronger image heterogeneity signal. To explore estimation dynamics, we vary $\nu \in \{0.01, 0.1, 1\}$.

The filter used in the convolution function of Equation 3 is visualized in Figure A.1, along with high and low responders from the set of images used in the simulation that we take from sub-Saharan Africa. We have some degree of model misspecification in our estimation model, as the way the data is generated is distinct from the estimation model; given this misspecification, we will examine the degree to which our model will recover key properties of the image-based causal heterogeneity. A visual depiction of the generative model for the simulation data is provided in Figure A.2.

Cluster Recovery Measure We compare the estimated effect clustering with an oracle baseline from the true, in practice unknown, τ_i 's. In particular, we first compute the oracle k -means clustering:

$$\tau(z)_{\text{Oracle}} = z^{\text{th}} \text{ center from the oracle } k\text{-means applied to the true (in practice unknown) } \tau_i\text{'s}$$

The clustering quality measure then compares the oracle with estimated cluster means:

$$\text{Cluster Recovery } R^2 = 1 - \frac{\sum_{z=1}^K \min_{z'} (\hat{\tau}(z) - \tau(z')_{\text{Oracle}})^2}{\sum_{z''=1}^K (\tau(z'')_{\text{Oracle}} - \bar{\tau}_{\text{Oracle}})^2},$$

where $\bar{\tau}_{\text{Oracle}}$ denotes the mean across the oracle cluster centers. This measure is equivalent to the R^2 in predicting the oracle cluster means from the estimated ones, where the ordering of the clusters has been arranged so that each oracle center is compared to its nearest estimated counterpart.

Simulation Results We see in the left panel of Figure 2 one representative posterior distribution over $Y_i(1) - Y_i(0)$ given estimated cluster information. We find that the estimated clusters capture the bimodality present in the true distribution of τ_i 's. In the right panel, we see that the cluster recovery measure for the Image-Type Differential Effects Model and TARNet clustering are similar in the low residual variance setting. In the high residual variance setting, the TARNet clustering struggles to recover the oracle cluster centers. The parsimonious Image-Type Effect Clustering Model here performs best at recovering the clustering of the treatment effects across the noise range. In Figure A.4, we see that the estimated ATEs are on average closer to the true value using the two image-type models (which use Model ATE Equivalence Regularization) compared to the TARNet approach.

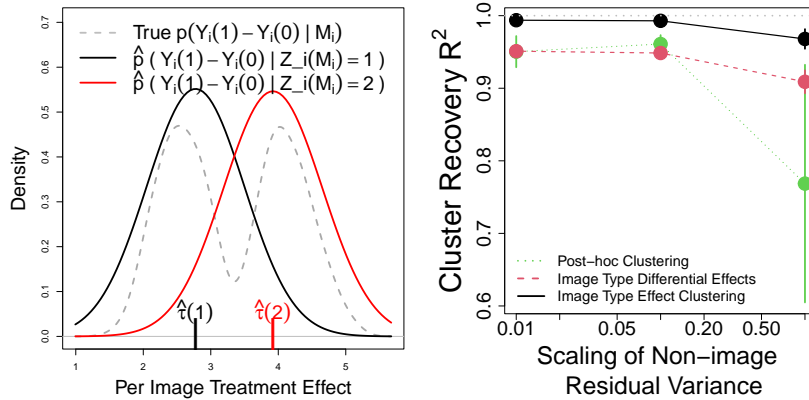


Figure 2: *Left.* Capturing the treatment effect heterogeneity. *Right.* Comparing our models.

5 Application to an Anti-Poverty Experiment in Uganda

Data In our application, we explore the effects of the anti-poverty experiment performed in Uganda and described in §1. The treatment variable is random assignment of small teams to receive grants

for business ventures. The outcome variable is an aggregate summary of skilled labor (see A.4.1) measured at the end of the experiment (two years after treatment assignment). Outcome and treatment data, available under CC0 1.0 license, are de-identified and were given voluntarily by subjects.

Pre-treatment image data is taken from Landsat. We use the Orthorectified ETM+ pan-sharpened data product. This product is derived using satellite imagery captured between 1998 and 2001 (about 10 years pre-intervention) and is processed so as to contain minimal cloud-cover. Reflectance is measured in the green, near-infrared, and short-wave infrared bands; resolution is 14.25 meters.

Empirical Results We fit the Image-Type Effect Cluster Model (details in A.6). We set the cluster number to two after finding that cluster probabilities become highly correlated with additional clusters. We plot in Figure 3 the top images having highest mean cluster probabilities. For each image, we also place a square around the top sensitivity regions as defined in §3.3. We see that the cluster treatment effect for cluster 1 is about 20% greater than cluster 2. This finding suggest that larger treatment effects are present for places having harsher terrain and less developed transportation network. This finding emerges when we plot the clustering on the land cover map of Uganda in Figure A.5. Geographically, many of the low responders are found in the harsh mountainous northern part of Uganda. We see in A.4 that the places having the most uncertainty in the cluster probabilities are locations characterized dominated by water features. In addition, we orthogonalize the potential outcomes using tabular information (see A.5), and the results remain similar: correlation between raw and non-orthogonalized cluster probabilities is 0.88. Because our results remain similar after orthogonalization, the Ugandan satellite images seem to supply independent CATE information that the original experimenters were unable to assess. Consequently, what our CATE-image analysis shows is that the causal effect of Ugandan youth groups is higher, if they also have live in historically well-connected neighborhoods. This is logical, as skilled labor tends to thrive in such hotspots.

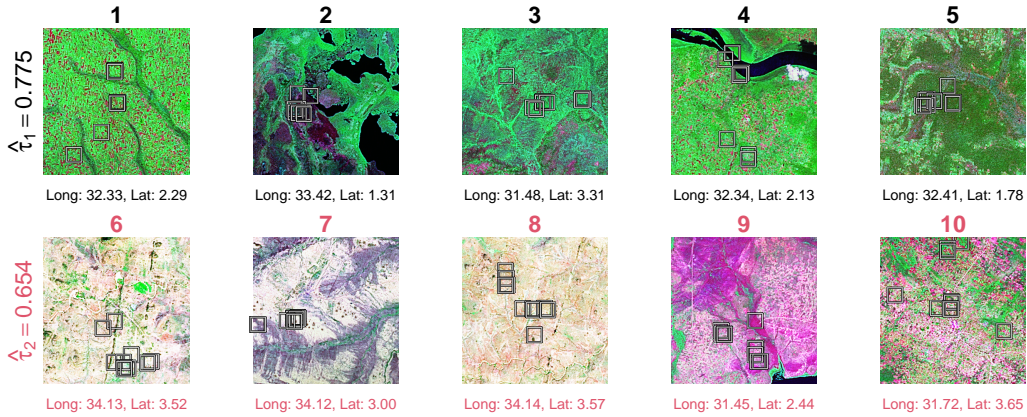


Figure 3: *Top.* High probability cluster 1 images. *Bottom.* High probability cluster 2 images.

6 Discussion and Conclusion

Limitations Our methods have certain limitations. First, they estimate heterogeneity clusters at the image level, but not for smaller segments of an image. This within-image heterogeneity segmentation would further improve interpretability. Second, our methods estimate heterogeneity with respect to an assumed baseline (i.e. the control intervention). While the choice of baseline is clear in most settings, in others, it may not be. In those unclear cases, the investigators may need to run the models using different baselines, depending on their needs, and compare results.

Societal Impact As demonstrated in our analysis of the Ugandan anti-poverty experiment, our method identifies possible heterogeneity not originally detected because the investigators did not have access to historical and geographical data—information imprinted in, for example, satellite images. Thus, our satellite-based methods have the potential to contribute to policy by complementing traditional RCT heterogeneity analysis based on tabular \mathbf{X}_i . Other applications where image data is omnipresent are precision agriculture, disaster relief, climate science, and medicine. More research and considerations of fairness are required to evaluate our methods in these settings.

Observational Setting Using experimental data has the benefit that effect estimates are confounding-free by design; effect heterogeneity can be studied independently of identification. Observational data are more plentiful but require adjustment (Rosenbaum et al., 2010). Our current methodology is not designed for that setting. For our method to remain unbiased, factors causal of the outcome would need to be well-captured by the image \mathbf{M}_i and the induced clustering Z_i . If a set of variables provides exchangeability with respect to potential outcomes $Y_i(0), Y_i(1)$ (Rosenbaum and Rubin, 1983), it could be incorporated directly as input to the model of $Y_i(0)$. Doing the same for τ_i would require conditioning on the clustering and on \mathbf{M}_i , making the analysis more complicated.

Concluding Remarks In this paper, we present principles and modeling strategies for analyzing image-based treatment effect heterogeneity using probabilistic image-type models. We derive some properties of this model and perform approximate inference using variational methods. Dynamics are explored via simulation and an anti-poverty field experiment from Uganda analyzed, where we seem to find some evidence of novel heterogeneity dynamics. \square

References

- Susan Athey and Guido Imbens. Recursive partitioning for heterogeneous causal effects. *Proceedings of the National Academy of Sciences*, 113(27):7353–7360, 2016.
- Susan Athey, Julie Tibshirani, and Stefan Wager. Generalized random forests. *The Annals of Statistics*, 47(2):1148–1178, 2019.
- Sourabh Balgi, Jose M. Pena, and Adel Daoud. Personalized Public Policy Analysis in Social Sciences using Causal-Graphical Normalizing Flows. *Association for the Advancement of Artificial Intelligence: AI for Social Impact track*, February 2022. URL <http://arxiv.org/abs/2202.03281>. arXiv: 2202.03281.
- Abhijit Banerjee, Abhijit V Banerjee, and Esther Duflo. *Poor economics: A radical rethinking of the way to fight global poverty*. Public Affairs, 2011.
- Christopher Blattman, Nathan Fiala, and Sebastian Martinez. Generating skilled self-employment in developing countries: Experimental evidence from uganda. *The Quarterly Journal of Economics*, 129(2):697–752, 2014.
- Marshall Burke, Anne Driscoll, David B. Lobell, and Stefano Ermon. Using satellite imagery to understand and promote sustainable development. *Science*, 371(6535):eabe8628, March 2021. ISSN 0036-8075, 1095-9203. doi: 10.1126/science.abe8628. URL <https://www.sciencemag.org/lookup/doi/10.1126/science.abe8628>.
- Daniel C. Castro, Ian Walker, Ben Glocker, Ian Walker, and Ben Glocker. Causality matters in medical imaging. *Nature Communications*, 11(1):3673, July 2020. ISSN 2041-1723. doi: 10.1038/s41467-020-17478-w. URL <https://www.nature.com/articles/s41467-020-17478-w>. Bandiera_abtest: a Cc_license_type: cc_by Cg_type: Nature Research Journals Number: 1 Primary_atype: Reviews Publisher: Nature Publishing Group Subject_term: Computational models;Data processing;Machine learning;Medical research;Predictive medicine Subject_term_id: computational-models;data-processing;machine-learning;medical-research;predictive-medicine.
- Krzysztof Chalupka, Pietro Perona, and Frederick Eberhardt. Visual Causal Feature Learning. Technical Report arXiv:1412.2309, arXiv, June 2015. URL <http://arxiv.org/abs/1412.2309>. arXiv:1412.2309 [cs, stat] type: article.
- Krzysztof Chalupka, Tobias Bischoff, Pietro Perona, and Frederick Eberhardt. Unsupervised Discovery of El Nino Using Causal Feature Learning on Microlevel Climate Data. Technical Report arXiv:1605.09370, arXiv, May 2016a. URL <http://arxiv.org/abs/1605.09370>. arXiv:1605.09370 [physics, stat] type: article.
- Krzysztof Chalupka, Frederick Eberhardt, and Pietro Perona. Multi-Level Cause-Effect Systems. In *Proceedings of the 19th International Conference on Artificial Intelligence and Statistics*, pages 361–369. PMLR, May 2016b. URL <https://proceedings.mlr.press/v51/chalupka16.html>. ISSN: 1938-7228.

- Nelson Cowan. The magical mystery four: How is working memory capacity limited, and why? *Current directions in psychological science*, 19(1):51–57, 2010.
- Roberta Cucca. Spatial segregation and the quality of the local environment in contemporary cities. In *Handbook of Urban Segregation*. Edward Elgar Publishing, 2020.
- Adel Daoud and Devdatt Dubhashi. Statistical modeling: the three cultures. *arXiv:2012.04570 [cs, stat]*, December 2020. URL <http://arxiv.org/abs/2012.04570>. arXiv: 2012.04570.
- Adel Daoud and Fredrik Johansson. Estimating treatment heterogeneity of international monetary fund programs on child poverty with generalized random forest. 2019.
- Adel Daoud, Felipe Jordan, Makkunda Sharma, Fredrik Johansson, Devdatt Dubhashi, Sourabh Paul, and Subhashis Banerjee. Using satellites and artificial intelligence to measure health and material-living standards in India. Technical Report arXiv:2202.00109, arXiv, December 2021. URL <http://arxiv.org/abs/2202.00109>. arXiv:2202.00109 [cs, econ, q-fin] type: article.
- Mingyu Ding, Zhenfang Chen, Tao Du, Ping Luo, Josh Tenenbaum, and Chuang Gan. Dynamic Visual Reasoning by Learning Differentiable Physics Models from Video and Language. In *Advances in Neural Information Processing Systems*, volume 34, pages 887–899. Curran Associates, Inc., 2021. URL <https://proceedings.neurips.cc/paper/2021/hash/07845cd9aefa6cde3f8926d25138a3a2-Abstract.html>.
- Peng Ding, Avi Feller, and Luke Miratrix. Randomization inference for treatment effect variation. *Journal of the Royal Statistical Society: Series B (Statistical Methodology)*, 78(3):655–671, 2016.
- Yarin Gal and Zoubin Ghahramani. Dropout as a bayesian approximation: Representing model uncertainty in deep learning. In *international conference on machine learning*, pages 1050–1059. PMLR, 2016.
- Max Goplerud, Kosuke Imai, and Nicole E Pashley. Estimating heterogeneous causal effects of high-dimensional treatments: Application to conjoint analysis. *arXiv preprint arXiv:2201.01357*, 2022.
- Michael Greenacre. Compositional data analysis. *Annual Review of Statistics and its Application*, 8: 271–299, 2021.
- Sander Greenland, Michael P Fay, Erica H Brittain, Joanna H Shih, Dean A Follmann, Erin E Gabriel, and James M Robins. On causal inferences for personalized medicine: How hidden causal assumptions led to erroneous causal claims about the d-value. *The American Statistician*, 74(3): 243–248, 2020.
- Robins JM Hernán MA. *Causal Inference: What If*. Boca Raton: Chapman & Hall/CRC, 2020.
- Günter J Hitsch and Sanjog Misra. Heterogeneous treatment effects and optimal targeting policy evaluation. *Available at SSRN 3111957*, 2018.
- Kosuke Imai and Marc Ratkovic. Estimating treatment effect heterogeneity in randomized program evaluation. *The Annals of Applied Statistics*, 7(1):443–470, 2013.
- Guido W Imbens and Donald B Rubin. *Causal inference in statistics, social, and biomedical sciences*. Cambridge University Press, 2015.
- Connor T Jerzak, Fredrik Johansson, and Adel Daoud. Estimating causal effects under image confounding bias with an application to poverty in africa. *arXiv preprint arXiv:2206.06410*, 2022.
- Jean Kaddour, Yuchen Zhu, Qi Liu, Matt J Kusner, and Ricardo Silva. Causal effect inference for structured treatments. *Advances in Neural Information Processing Systems*, 34, 2021a.
- Jean Kaddour, Yuchen Zhu, Qi Liu, Matt J. Kusner, and Ricardo Silva. Causal Effect Inference for Structured Treatments. *Advances in Neural Information Processing Systems*, 34, 2021b.
- Nathan Kallus. Deepmatch: Balancing deep covariate representations for causal inference using adversarial training. In *International Conference on Machine Learning*, pages 5067–5077. PMLR, 2020.

- Shiho Kino, Yu-Tien Hsu, Koichiro Shiba, Yung-Shin Chien, Carol Mita, Ichiro Kawachi, and Adel Daoud. A scoping review on the use of machine learning in research on social determinants of health: Trends and research prospects. *SSM - Population Health*, 15:100836, September 2021. ISSN 2352-8273. doi: 10.1016/j.ssmph.2021.100836. URL <https://www.sciencedirect.com/science/article/pii/S2352827321001117>.
- Sören R Künzel, Jasjeet S Sekhon, Peter J Bickel, and Bin Yu. Metalearners for estimating heterogeneous treatment effects using machine learning. *Proceedings of the national academy of sciences*, 116(10):4156–4165, 2019.
- David Lopez-Paz, Robert Nishihara, Soumith Chintala, Bernhard Scholkopf, and Leon Bottou. Discovering Causal Signals in Images. pages 6979–6987, 2017. URL https://openaccess.thecvf.com/content_cvpr_2017/html/Lopez-Paz_Discovering_Causal_Signals_CVPR_2017_paper.html.
- Christos Louizos, Uri Shalit, Joris M Mooij, David Sontag, Richard Zemel, and Max Welling. Causal Effect Inference with Deep Latent-Variable Models. In *Advances in Neural Information Processing Systems*, volume 30. Curran Associates, Inc., 2017. URL <https://proceedings.neurips.cc/paper/2017/hash/94b5bde6de88ddf9cde6748ad2523d1-Abstract.html>.
- Alexander R Luedtke and Mark J van der Laan. Super-learning of an optimal dynamic treatment rule. *The international journal of biostatistics*, 12(1):305–332, 2016.
- Razieh Nabi, Joel Pfeiffer, Murat Ali Bayir, Denis Charles, and Emre Kıcıman. Causal inference in the presence of interference in sponsored search advertising. *arXiv preprint arXiv:2010.07458*, 2020.
- Xinkun Nie and Stefan Wager. Quasi-oracle estimation of heterogeneous treatment effects. *Biometrika*, 108(2):299–319, 2021.
- Michael Oberst, Nikolaj Thams, Jonas Peters, and David Sontag. Regularizing towards causal invariance: Linear models with proxies. In *International Conference on Machine Learning*, pages 8260–8270. PMLR, 2021.
- Christopher J Paciorek. The importance of scale for spatial-confounding bias and precision of spatial regression estimators. *Statistical science: a review journal of the Institute of Mathematical Statistics*, 25(1):107, 2010.
- Paavo Parmas and Masashi Sugiyama. A unified view of likelihood ratio and reparameterization gradients. In *International Conference on Artificial Intelligence and Statistics*, pages 4078–4086. PMLR, 2021.
- Nick Pawlowski, Daniel C. Castro, and Ben Glocker. Deep Structural Causal Models for Tractable Counterfactual Inference. *arXiv:2006.06485 [cs, stat]*, October 2020. URL <http://arxiv.org/abs/2006.06485>. arXiv: 2006.06485.
- Judea Pearl. *Causality*. Cambridge university press, 2009.
- Judea Pearl and Elias Bareinboim. External validity: From do-calculus to transportability across populations. In *Probabilistic and Causal Inference: The Works of Judea Pearl*, pages 451–482. 2022.
- Vikas Ramachandra. Causal inference for climate change events from satellite image time series using computer vision and deep learning. *arXiv preprint arXiv:1910.11492*, 2019.
- Rajesh Ranganath, Sean Gerrish, and David Blei. Black box variational inference. In *Artificial intelligence and statistics*, pages 814–822. PMLR, 2014.
- Paul R Rosenbaum and Donald B Rubin. The central role of the propensity score in observational studies for causal effects. *Biometrika*, 70(1):41–55, 1983.
- Paul R Rosenbaum, PR Rosenbaum, and Briskman. *Design of observational studies*, volume 10. Springer, 2010.

- Donald B Rubin. Causal inference using potential outcomes: Design, modeling, decisions. *Journal of the American Statistical Association*, 100(469):322–331, 2005.
- Bernhard Schölkopf, Francesco Locatello, Stefan Bauer, Nan Rosemary Ke, Nal Kalchbrenner, Anirudh Goyal, and Yoshua Bengio. Towards Causal Representation Learning. *arXiv:2102.11107 [cs]*, February 2021. URL <http://arxiv.org/abs/2102.11107>. arXiv: 2102.11107.
- Uri Shalit, Fredrik D Johansson, and David Sontag. Estimating individual treatment effect: generalization bounds and algorithms. In *International Conference on Machine Learning*, pages 3076–3085. PMLR, 2017.
- Koichiro Shiba, Adel Daoud, Hiroyuki Hikichi, Aki Yazawa, Jun Aida, Katsunori Kondo, and Ichiro Kawachi. Heterogeneity in cognitive disability after a major disaster: A natural experiment study. *Science advances*, 7(40):eabj2610, 2021.
- T Westling and TH McCormick. Beyond prediction: A framework for inference with variational approximations in mixture models. *Journal of Computational and Graphical Statistics*, 28(4): 778–789, 2019.
- Kexin Yi, Chuang Gan, Yunzhu Li, Pushmeet Kohli, Jiajun Wu, Antonio Torralba, and Joshua B. Tenenbaum. CLEVRER: CoLLision Events for Video REpresentation and Reasoning. Technical Report arXiv:1910.01442, arXiv, March 2020. URL <http://arxiv.org/abs/1910.01442>. arXiv:1910.01442 [cs] type: article.
- Qingyuan Zhao, Dylan S Small, and Ashkan Ertefaie. Selective inference for effect modification via the lasso. *arXiv preprint arXiv:1705.08020*, 2017.

A Appendix

A.1 Supplementary Information for the Image-Type Probabilistic Models

A.1.1 Deriving the Conditional Distribution, $Y_i(1) - Y_i(0) | Z_i = z$

Using the model outlined in §3.1, conditioning on τ_i , and exploiting Normality,

$$\{Y_i(1) - Y_i(0) \mid Z_i = z, \tau_i\} \sim \mathcal{N}(\tau_i, \sigma_{0,z}^2 + \sigma_{1,z}^2)$$

Integrating out τ_i :

$$\begin{aligned} p(Y_i(1) - Y_i(0) = d_i \mid Z_i = z) &= \int_{-\infty}^{\infty} p(Y_i(1) - Y_i(0) = d_i \mid Z_i = z, \tau_i) p(\tau_i \mid Z_i = z) d\tau_i \\ &= \int_{-\infty}^{\infty} \frac{1}{\sqrt{2\pi(\sigma_{0,z}^2 + \sigma_{1,z}^2)}} \exp\left\{\frac{-(d_i - \tau_i)^2}{2(\sigma_{0,z}^2 + \sigma_{1,z}^2)}\right\} \\ &\quad \times \frac{1}{\sqrt{2\pi\sigma_{\tau,z}^2}} \exp\left\{\frac{-(\tau_i - \mu_{\tau,z})^2}{2\sigma_{\tau,z}^2}\right\} d\tau_i \\ &= \frac{1}{\sqrt{2\pi((\sigma_{0,z}^2 + \sigma_{1,z}^2) + \sigma_{\tau,z}^2)}} \exp\left\{\frac{-(d_i - \mu_{\tau,z})^2}{2((\sigma_{0,z}^2 + \sigma_{1,z}^2) + \sigma_{\tau,z}^2)}\right\}. \end{aligned}$$

Therefore,

$$\{Y_i(1) - Y_i(0) \mid Z_i = z\} \sim \mathcal{N}(\mu_{\tau,z}, \sigma_{0,z}^2 + \sigma_{1,z}^2 + \sigma_{\tau,z}^2).$$

A.1.2 Additional Modeling Details

The real representation of the uncertainties are all drawn from Gaussians with mean and variance scaled indexed to z ; the non-negativity of the variance is enforced through the softplus transformation (where $\text{softplus}(x) = \log(1 + \exp(x))$).

A.2 Causal Regularization

In a simplified model where the distribution of each potential outcome, $Y_i(0)$ and $Y_i(1)$, is characterized by a Gaussian mixture with means $\mu_{t,z}$ for $z \in \{1, 2, \dots, K\}$, Equation 2 can be made to hold exactly through parameterization. In particular, we would like to solve:

$$\sum_{z=1}^K \hat{\tau}(z) \widehat{\Pr}(Z(\mathbf{M}) = z) - \hat{\tau} = 0$$

Under this simplified model, $\hat{\tau}(z) = \hat{\mu}_{1,z} - \hat{\mu}_{0,z}$, so

$$\begin{aligned} & \sum_{z=1}^K (\hat{\mu}_{1,z} - \hat{\mu}_{0,z}) \widehat{\Pr}(Z(\mathbf{M}) = z) - \hat{\tau} = 0 \\ & (\hat{\mu}_{1,z=1} - \hat{\mu}_{0,z=1}) \widehat{\Pr}(Z(\mathbf{M}) = 1) + \sum_{z=2}^K (\hat{\mu}_{1,z} - \hat{\mu}_{0,z}) \widehat{\Pr}(Z(\mathbf{M}) = z) - \hat{\tau} = 0 \end{aligned}$$

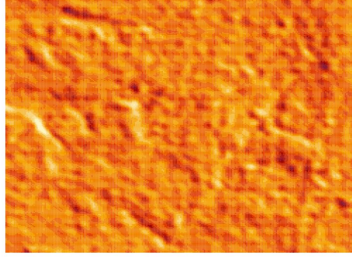
which implies

$$\hat{\mu}_{0,z=1} = \hat{\mu}_{1,z=1} - \left(\hat{\tau} - \sum_{z=2}^K (\hat{\mu}_{1,z} - \hat{\mu}_{0,z}) \widehat{\Pr}(Z(\mathbf{M}) = z) \right) \widehat{\Pr}(Z(\mathbf{M}) = 1)^{-1}.$$

Thus, in some modeling contexts, the exact non-parametric ATE can be recovered in the clustering model by parametrization.

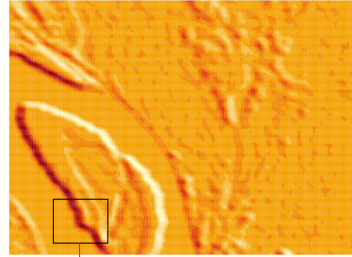
A.3 Simulation Details

Low Responder



No neighborhood of similarity to heterogeneity-generating pattern

High Responder



Neighborhood with high similarity to heterogeneity-generating pattern

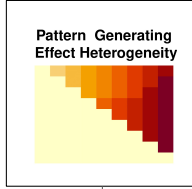


Figure A.1: Illustration. In the center, we see the image pattern used in generating the heterogeneity response in the simulation design of §4. In the left panel, we see an image having no regions of strong similarity to the heterogeneity-generating pattern (leading to a low treatment effect); in the right panel, we see an image with many regions of strong similarity to the heterogeneity-generating pattern (leading to a high treatment effect).

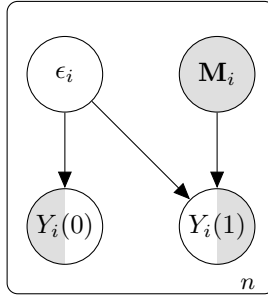


Figure A.2: *Left panel.* Stylized schematic depiction of the simulation model. Note that this model is not the same as the probabilistic estimation model (i.e. we have some degree of misspecification in our probabilistic models).

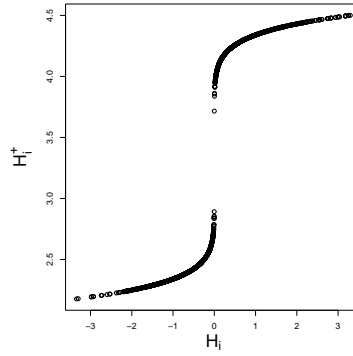


Figure A.3: Illustration of the non-linear transformation used in the simulation in generating H_i^+ from H_i .

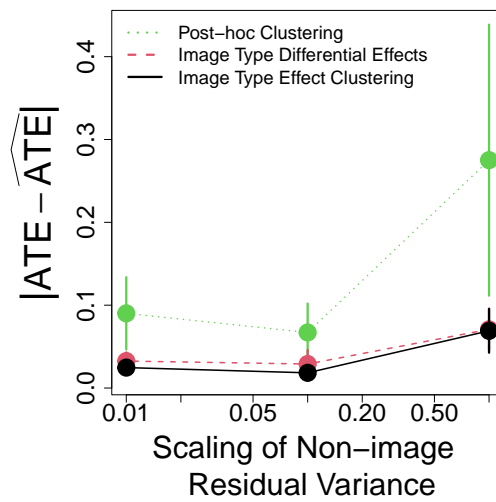


Figure A.4: ATE recovery is improved with the two image-type cluster models fit using the Model ATE Equivalence Regularization Term.

A.4 Supplementary Analyses for the Application

A.4.1 Additional Data Description

Satellite data is obtained for the smallest geographic locality associated with a given experimental unit. Place names were geo-referenced using OpenStreetMap data. When geo-referencing failed, we use the geometric center for the layer associated with the geographic unit as our focal point for the given unit. Satellite information was then obtained for a cube around focal points with side lengths of 5000 meters. For the skilled work outcome, we take the scaled sum of the log hours worked in the last 7 days by experimental units in skilled or highly skilled trades.

A.4.2 Additional Analyses

Table 1: Correlation of estimated image cluster 1 probabilities with key tabular covariates.

	Correlation
Urban	-0.27
Longitude	0.31
Latitude	-0.40
Female indicator	0.01
Human capital score	-0.01

A.5 Empirical Analysis with Orthogonalized Potential Outcomes

We orthogonalize outcomes by, in line with the original experimental analysis, fitting a regression model predicting the outcome using main treatment effects and interactions between treatment and gender, treatment and baseline human capital, and treatment and baseline business capital (as well as the main effect terms for the associated interaction). We find a 0.88 correlation between the cluster probabilities using the orthogonalized and raw outcomes.

A.6 Model Implementation Details

In the implementation of our models using Bayesian CNN arms, we leave the number of hidden layers, filter size, and so forth as parameters that can be set by investigators, although we seek to keep the computational overhead low so as to increase the usefulness of these modeling strategies for investigators having limited supercluster access.

In our application, we use four convolutional layers (filter size 3), separated by max pooling layers (2×2). Each convolutional layer applies 96 filters. Bottleneck projection layers are used after each convolutional layer, projecting the 96 dimensions down to 3 to keep the number of parameters low. Batch normalization layers are used across the feature dimension before each projection or convolution. The swish activation is used. We apply the Gumbel-Softmax to approximate the random categorical sampling with inverse temperature set to 1. We set $\lambda = 0.01$. With this model structure, each batch sample of 20 units takes about one second on a single Apple M1 GPU using Metal-optimized tensorflow 2.8. The full simulations with 10 Monte Carlo iterations per design setting take about 12 hours on this hardware.

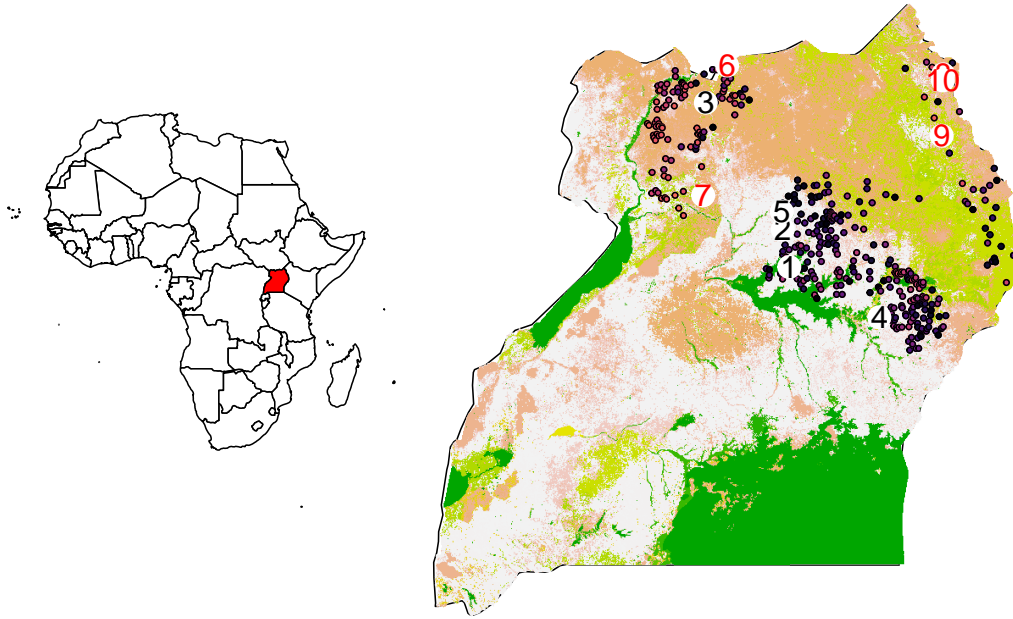


Figure A.5: Location of the top 5 cluster 1 and 2 localities. A selection of the other experimental units are displayed visually as well, with the color of the point related to the cluster probability.

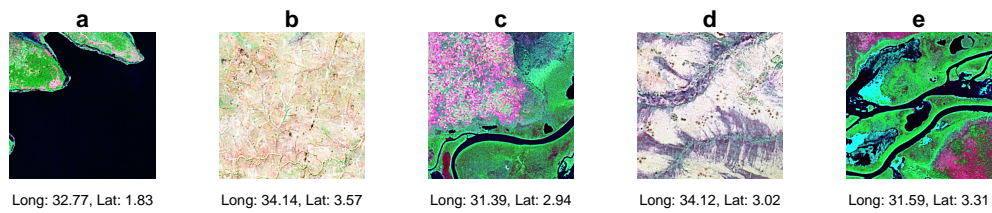


Figure A.6: Images with most uncertainty in cluster probabilities from the main empirical analysis.

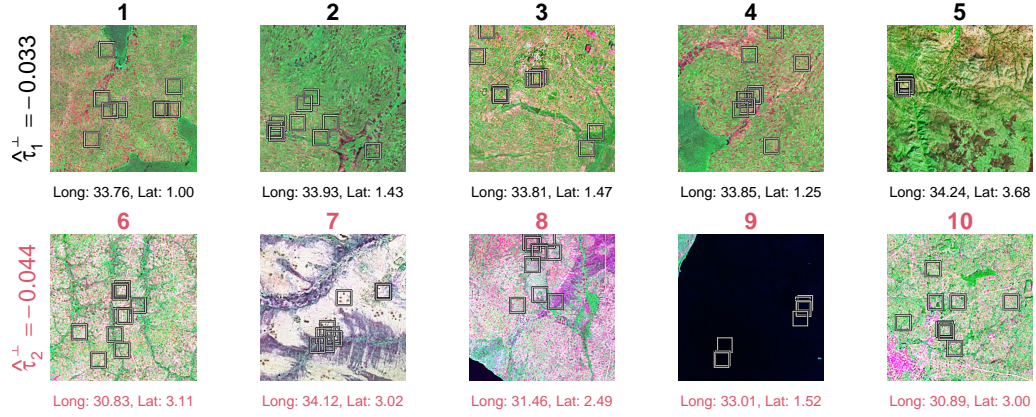


Figure A.7: *Top*. High probability cluster 1 images using orthogonalized outcomes. *Bottom*. High probability cluster 2 images using orthogonalized outcomes. Note that cluster labels are not identified (so the cluster labels, “1” and “2”, should not be interpreted as meaningful).

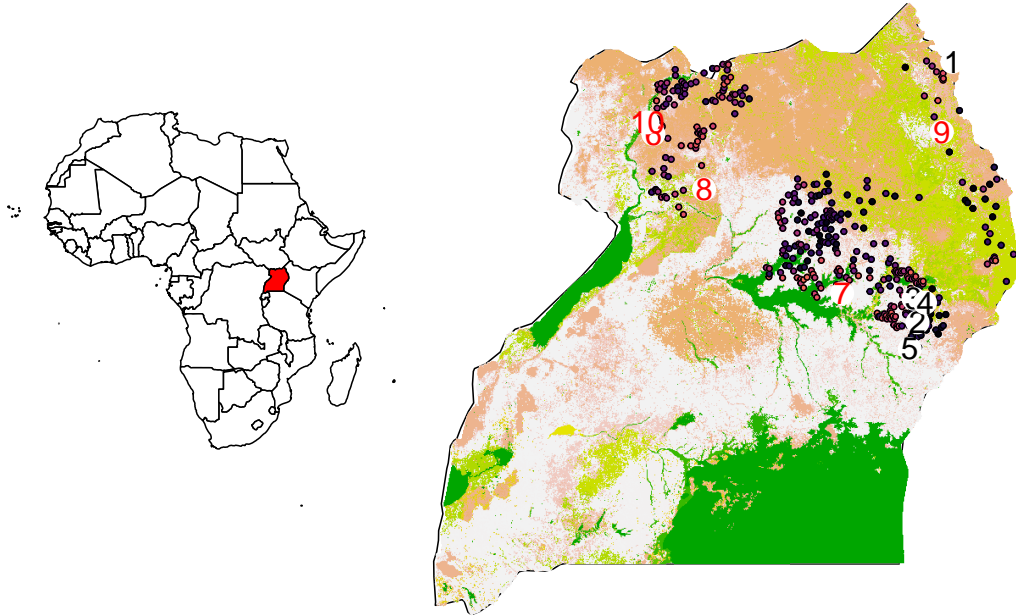


Figure A.8: Location of the top 5 cluster 1 and 2 localities using the model fit on tabular orthogonalized outcomes. Correlation between cluster probabilities using the raw and orthogonalized outcomes is 0.88.